Normal Shock-Boundary Layer Interactions in Transonic Intakes at High Incidence

A. Coschignano* and H. Babinsky[†]
Department of Engineering, University of Cambridge, Cambridge, CB2 1PZ, UK

C.Sheaf[‡] and G.Zamboni [§]
Installation Aerodynamics, Rolls Royce Plc., Derby, DE24 8BJ, UK

During high-incidence manoeuvres, shock-wave boundary layer interactions can develop over transonic inlet lower lips, significantly impacting aerodynamic performance. Here, a novel experimental rig is used to investigate the nature and severity of these interactions for a typical high incidence scenario. Furthermore, we explore the sensitivity to changes in angle of incidence and mass flow rate, as potentially experienced across off-design operations.

The reference flow-field, informed by typical climb conditions, is defined by an incidence of 23° and a free stream Mach number M=0.435. The lower lip flow is characterised by a rapid acceleration around the leading-edge and a M≈1.4 shock ahead of the intake diffuser. Overall, this flow-field is found to be relatively benign, with minimal shock-induced separation. Downstream of the interaction, the boundary layer recovers a healthy profile ahead of the nominal fan location. Increasing incidence by 2°, the separation becomes noticeably larger and unsteadiness develops. Detrimental effects are exacerbated at an even higher incidence of 26°. Increasing the mass flow rate over the lip by up to 15% of the initial value has minor effects on performance and is not found to inhibit the boundary layer profile recovery.

Nomenclature

α Angle of incidence

δ Boundary layer thickness

δ^* Boundary layer displacement thickness

θ Boundary layer momentum thickness

c Intake chord length

H   Shape factor

L^* Interaction length

---

*Research Associate, Department of Engineering, University of Cambridge.
[†]Professor of Aerodynamics, Department of Engineering, University of Cambridge, AIAA Associate Fellow.
[‡]Installation Aerodynamics, Rolls Royce Plc.
[§]Installation Aerodynamics, Rolls Royce Plc.

$\dot{m}$ Mass flow

$m(x)$ Super ellipse x exponent

n Super ellipse y exponent

M   Mach number

P   Pressure

Re Reynolds number (based on lip thickness)

s Stream-wise distance along surface

t_m Intake maximum thickness

U Flow velocity

x Stream-wise direction, parallel to lab floor

y Vertical direction, normal to surface model, unless otherwise stated

z Span-wise direction.

AR   Intake aspect ratio

LDV   Laser Doppler velocimetry

PSP   Pressure sensitive paint

SBLI   Shock-wave boundary layer interaction

VEP Virtual Engine Plane, $x=2.4t_m, baseline$

Subscript

0   Stagnation value

1   Property upstream of the shock

e Free-stream property

l Lower channel, usually referred to mass flows

i Incompressible property

u Upper channel, usually referred to mass flows

I. Transonic inlets at incidence

In recent years, pressing environmental concerns are leading the charge towards more efficient aerodynamic design. The Advisory Council for Aeronautics Research in Europe (ACARE) has set the ambitious goal of reducing, by 2050, CO_2 emissions by 75% compared to the start of the century [1]. Alongside improvements in engine thermal efficiency, manufacturers are pursuing new inlet designs in order to maximise aerodynamic performance and pressure recovery. Although in a aircraft mission level flight dominates, the inlet is primarily configured for off-design operation, such as

ground crosswind and high incidence, to ensure the fan system is supplied with an appropriate quantity and uniform quality of airflow throughout the aircraft operating envelope, including emergency manoeuvring, such as when the aeroplane is approaching stall, in order to aid flight path recovery [2].

During high-incidence manoeuvring, the performance envelope of a wing mounted engine nacelle is currently bounded by the onset of flow distortion around the lower lip. In this scenario, the stagnation point is generally located on the outer surface of the nacelle. As incidence or mass flow rate increase, two main types of separation are commonly reported: flow separation in the diffuser or at the highlight (inlet leading edge), with the latter indicating a fully stalled intake [3]. A schematic depiction of the two separation types is presented in Figure 1a-b. Separation at the highlight is generally caused by the strong acceleration around the nose followed by severe adverse pressure gradients defining the post-highlight re-compression phase. On the other hand, separation in the diffuser is caused by the adverse pressure gradients downstream of the throat plane where the flow speed is reduced ahead of the fan [4]. Similar flow distortion is observed during crosswind operation in both wing and empennage mounted nacelles.

Previous experimental studies [3, 4], analytical models and computations [5–7] have mostly been concerned with the onset of highlight separation at both high and low speed. At lower speed, the incidence at which lip separation occurs was found to increase with mass flow rate. However, high speed experiments by Jakubowski *et al.* [4] and Miller *et al.* [3] found the separation boundary to drop sharply for high mass flow rates (i.e.: yielding an average Mach number at the throat plane in excess of $M_t \geq 0.7$). At these conditions, they also reported a reduction in overall total pressure recovery. Observing static pressure distribution over the lower lip at incidence levels preceding highlight separation, Jakubowski *et al.* attributed this behaviour to the pronounced over-speed around the lower lip resulting in pockets of supersonic flow leading to shock-induced separation within the inlet. It was proposed that this shock-wave, and associated separation, could propagate upstream towards the highlight, eventually resulting in a fully separated inlet [4]. However, due to hysteresis and poor resolution of these early experiments, this terminal shock-wave and the nature of its interaction
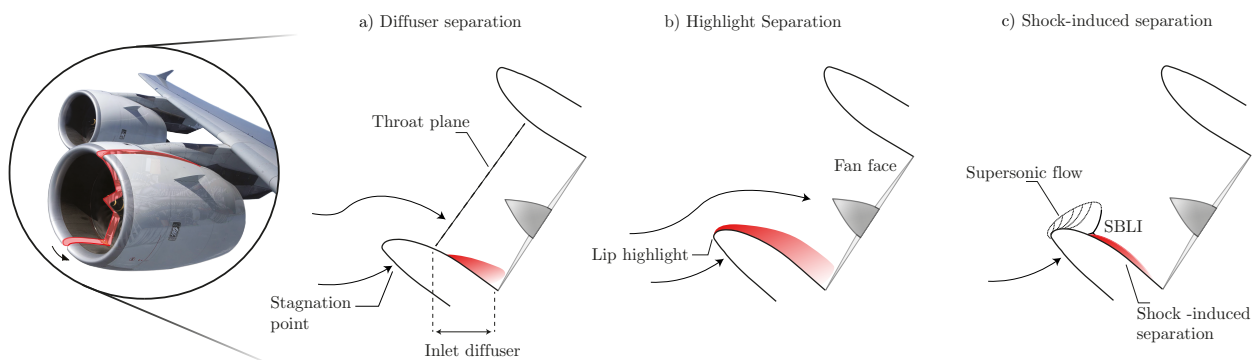

Fig. 1 Schematics of an inlet cross section showing: a) Flow separating in an intake diffuser during high incidence flight; b) separation occurring at the lip highlight (intake stall). c) Shock induced separation over the lower lip.

with the boundary layer over the lower lip could not be characterised. Recent computational efforts by Cao *et al.* [8] and experimental investigations by Makuni *et al.* [9]confirmed the flow topology suggested by Jakubowski *et al.* and reported a normal shock over the lower lip, as schematically shown in Figure 1c. Characterisation of the shock-wave boundary layer interaction was, however, beyond the scope of both Cao *et al.* and Makuni *et al.* [8, 9].

As larger engines are being pursued by manufacturers to improve overall efficiency [10], in order to accommodate the larger turbofans a re-design of the nacelle becomes necessary. In light of the intake re-shaping challenge, understanding the onset of detrimental effects associated with high incidence flight might contribute to improved lip designs. Ideally, this would allow engine inlets to operate more efficiently over a wider range of conditions, including limit high incidence manoeuvring and off-design scenarios involving SBLIs, which remain to be addressed in the context of engine inlets at high-incidence.

This paper aims to characterise the shock-wave boundary layer interaction developing over the lower lip in scenarios representative of high incidence operations but before the onset of full lip separation. This is done experimentally by using a unique rig described in §II. The target flow-field is defined by a ~M=1.4 normal shock with an inflow characterised by a relatively high free-stream Mach number ($M_0 \geq 0.4$) and an incidence level of 23° (§III). Subsequently, the flow response to increasing internal mass flow rate (§IV) and the consequences of increments in angle of incidence, by 2 and 3 degrees respectively (§V), are also explored.

II. Experimental configuration and methodology

A. Target flow-field and working section design

The experimental set-up is nominally 2D for a number of reasons. First, the problem can be simplified by noting that high incidence operation reduces the area of aerodynamic interest to the lower lip only. It is assumed that the length-scale of tangential changes along the nacelle circumference is of the order of its curvature radius. This is noticeably larger than the lip radius and thickness, which could be considered representative length-scales of the stream-wise and normal changes along the lip. Thus, considering only a cross section along the centre span of the intake, the lower lip is effectively treated like a two dimensional aerofoil.

To delimit the experimental domain, a stream-tube geometry in the symmetry plane was extracted from 3D RANS computations of a typical engine flow and used to define the wind tunnel working section depicted in Figure 2. Subsequently, the set-up was fine tuned, as described in detail in §II.C, in order to obtain a pressure distribution matching wind tunnel test data on a 3D nacelle deemed representative of high-incidence manoeuvring.

The lip geometry used here is a generic lip shape (defined in §II.E) designed to generate a pressure distribution, shock strength and location comparable with current design practice.
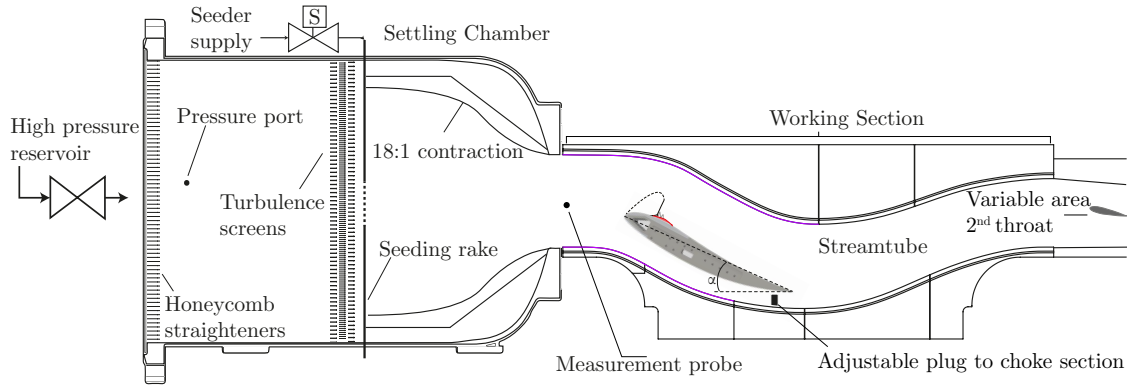
B. CUED blow down wind-tunnel

Fig. 2 Representation of the blow-down wind tunnel facility. Flow from left to right. Stream-tube design based on computed flow streamlines selected by Makuni [9].

The blow-down wind-tunnel assembly is schematically depicted in Figure 2. The wind-tunnel is powered by two 50 kW compressors. The flow is fed from the compressors into the settling chamber, where it is passed through a number of flow straighteners and turbulence grids before a 18:1 contraction. The entry Mach number is varied by adjusting the effective area of the second throat where the flow is chocked by means of an aerofoil (see Figure 2). Changing the total pressure allows some degree of variation in Reynolds number.

The 114 mm wide, 445 mm long model divides the working section into two channels, bounded by the solid upper and lower walls. Altering the ratio between the mass flow rates in each channel provides an effective way to control a third variable: the engine mass flow demand. In a real intake, when engine mass flow rate varies, so does the stagnation streamline dividing the flow going into the intake from that spilled along the outer nacelle. During high incidence operation, this streamline comes to rest on the outer surface of the lip. As the amount of air captured by the intake increases, the stagnation streamline shifts further aft on the lower surface. In the experimental facility, this is replicated by using a choking rod in the lower channel as highlighted in Figure 2. The latter allows a fine control ($\Delta \dot{m}_l < 0.1\% \dot{m}$) of the mass flow discharged via the lower passage. To investigate the response to stagnation streamline changes, the overall mass flow is kept constant at the reference value while the mass flow rate through the lower passage is progressively reduced. This forces a greater proportion of the mass flow inside the upper channel, effectively mimicking a greater demand by a high bypass turbofan engine. Three increases in $\dot{m}_u$ have been considered in this investigation, namely $5 \pm 0.1\%$, $10 \pm 0.2\%$ and $15 \pm 0.3\%$ over the reference value. The model incidence can be adjusted between $23° \leq \alpha \leq 29°$.

C. Matching the target flow-field - Reference operating conditions

This section presents the operating parameters of the current facility that result in a flow-field closely matching a typical high-incidence condition.

A Reynolds number (based on maximum lip thickness and inflow velocity) $Re_t = 1.10 \times 10^6$, representative of a full scale, small sized engine at sea level, is used to achieve a good compromise between dynamic similarity and run time. This value is obtained with a stagnation pressure of 211kPa. To match the 3D tests pressure distribution, the model incidence was set at 23° and the entry Mach number set to $M_\infty = 0.435 \pm 0.0005$. These are both indicative of edge of the envelope high incidence operations. The choking rod is set so that ~74% of the total mass flow is discharged via the upper channel. The operating conditions are summarised in Table 1.

A number of off-design conditions are also explored. However, for practical reasons the geometry of the stream-tube defining the working section, based on stream-lines of the baseline flow-field extracted from a RANS CFD solution, was kept constant throughout the whole investigation. It can be argued that every operating point requires a new stream-tube geometry as the flow streamlines may change. Although an effect of the stream-tube geometry might be expected, this should not affect the main conclusions for a number of reasons: near the area of interest, the streamlines do not show a very pronounced curvature; moreover, at the design stage the upper bound of the working section was chosen to be sufficiently far from the supersonic region [9].

Furthermore, the changes in operating conditions around the design point are relatively minor: the highest increase in incidence from the baseline value is of only 3°. Moreover, the maximum increase in upper channel mass flow rate is limited to 15% of the initial value.

Table 1   Tunnel entry conditions for reference scenario

$\dot{m}$ (kg/s)	M_{entry}	α (deg.)	P_0 (kPa)	T_0 (K)	$\frac{\dot{m}_u}{\dot{m}_l}$	Re_t
8.68	0.435	23	211.6	290±4	~3.8	$\sim 10^6$

D. Experimental methods and errors

A Schlieren technique is used to visualize the features typical of compressible flow-fields. A horizontal knife edge is used and the images were captured at a rate of 4000fps at a resolution of 1024×512 pixels.

Surface pressure measurements in the centre-span are taken using tappings connected via tubing to a differential pressure transducer. Though small in diameter, the presence of a cavity can result in an over-prediction of static pressure by approximately 0.5%-1.0% according to Rayle [11]. The accuracy of the transducer is rated at ±0.05% of the full scale.

A number of these pressure readings are used to calibrate pressure sensitive paint (PSP). According to Gregory *et al.* [12], a minimum of 5 different known pressure values are usually sufficient to minimise error. In the current investigation, the mean deviation between the values extracted form the paint and that measured using the surface taps is found to be ranging from approximately 2% to a maximum of 4%.

Flow velocities in the tunnel centre-span are measured using a two component Laser Doppler Velocimetry

(LDV) system. The ellipsoidal working volume measures 130μm in diameter. Paraffin particles, with a diameter of approximately 0.5μm [13], are used to seed the flow. The laser emitting head and receiving optics are mounted on a three-axis traverse. The signal is sampled at an optimised variable rate to exploit a full signal cycle leading to a typical measurement accuracy, as stated by the manufacturer, of $\pm 0.1\%$ of U_{max} (~580m/s) [14]. In addition the emitting head is oriented at an angle $\beta = 8.5°$ from the horizontal. A component of the span-wise velocity, w, therefore affects the measurement of vertical velocity component. On the symmetry plane, where measurement are taken, w is expected to be one order of magnitude lower than v. As a consequence of this and of the small angle, the error in v is expected to be just above 1%. The stream-wise velocity component u is unaffected by β.

The other source of uncertainty is related to velocity bias. According to the findings of both McLaughlin *et al.* [15] and Buchhave *et al.* [16], the error is expected to be between 5% and 10% of U'. For the current investigation the error due to velocity bias is not expected to exceed 4% near the wall (based on the maximum measured value of $U' = 0.4U$). The vast majority of measurements are expected to have an average uncertainty around 1.5%.

Velocity measurements are used to estimate the incompressible boundary layer integral properties, which relies on integration of the velocity profile from the wall to the boundary layer edge. However, the measurement probe is of finite size and measuring any closer than 0.2mm from the wall is infeasible. Furthermore, numerically integrating over discrete data points can yield significant error. To address these shortcomings, an analytical boundary layer profile is fitted to the data points before integration.

The model by Sun & Childs [17], which builds on the classical linear combination of the law of the wall and Coles' wake function [18], has been used in the Cambridge facility for several years. Sun & Childs's models is valid down to $y^+ \approx 100$. For the buffer and viscous layers, the relationship proposed by Musker is used [19] to obtain complete solution for $0 \leq y \leq \delta$. The integral parameters can be calculated by simple numerical integration. A comprehensive investigation of the validity of this method has been performed by Titchener *et al.* [20]. The main sources of errors were found to be the resolution of discrete data points and misalignment of the wall position. In particular, the number of points necessary for the error to be $\leq 5\%$ is inversely proportional to the boundary layer shape factor but a minimum of 20 points inside the boundary layer is sufficient to achieve an error under 5% for a range of shape factors. This condition is generally satisfied in this investigation. Overall, the error is expected to be $< 2\%$ for the largest kinematic shape factor and $< 5\%$ for the thinnest, healthiest, boundary layers.

Wall offset was found to cause a significant error in integral parameters [20]. A small misalignment of $\Delta y/\delta$ of the order of 0.01 yields an error exceeding 5%. For the worst case scenario, defined by a thickness $\delta = 1.98$ mm, the wall location is accurate within $\Delta y/\delta \leq 0.005$. This places the outer error boundary to $\epsilon \leq 2\%$.

A summary of experimental error is given in Table 2.

Table 2   Summary of experimental errors

Flow property	Source	Error
Stagnation pressure P_0		
	pressure transducer	$\pm 0.05\%$
	settling chamber velocity (8m/s)	-0.04%
Static pressure P		
	pressure transducer	$\pm 0.05\%$
	orifice geometry - subsonic	$\pm 0.50\%$
	orifice geometry - supersonic	$\pm 1.00\%$
	pressure sensitive paint	$\pm 2.00\%$
Velocity		
	LDV processor resolution	$\pm 0.0015\%$
	Doppler frequency detection	$\pm 0.10\%$
	velocity bias near the wall	$+1.50\%$
	emitter angle, u	N/A
	emitter angle, v	$\pm 1\%$
Integral Parameters (after [20])		
	Number of discrete measurements	$\pm 2 - 5\%$
	Wall misalignment	$\pm 2\%$

E. Intake Lip Design

The intake lip has been designed by using a modified super ellipse profile as used by Lin [21] and Schrader [22], amongst many, for flat plate boundary layers investigations. Mathematically, a modified super ellipse is defined as:

$$\left(\frac{x-a}{a}\right)^m + \left(\frac{y}{b}\right)^n = 1 \tag{1}$$

with

$$m_{(x)} = 2 + \left(\frac{x}{a}\right)^2 \tag{2}$$

where a and b are the major and minor axis of the ellipse, respectively controlling the position and the size of the ellipse co-vertex. In intake terms, this point indicates where the intake is at its thickest, i.e.: the throat. Figure 3 depicts the coordinate system (originating at the lip highlight) and illustrates how the parameters defined in Equation 1 relate to the design of a real intake lip. The ratio a/b is defined as the aspect ratio AR of the ellipse. Its powers, on the other hand, set the locus of the point of maximum curvature. The current lip profile, highlighted in red in Figure 3 is defined by an aspect ratio $AR = 2.75$ and a value of $n = 2$.

This type of ellipse results in a continuous reduction in curvature from the highlight to the throat. Downstream of this, the geometry was tailored to replicate a typical diffuser shape. The mean diffuser angle, averaged between the
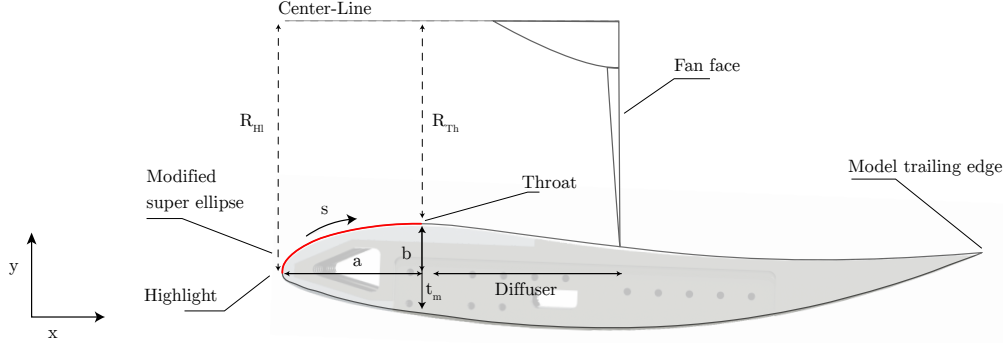
Fig. 3 Cross section of the model depicting the intake geometry definition, modified super ellipse in red. Coordinate s is defined as arc length along the lip.

throat and the nominal fan face, is -3.85° from the horizontal. The maximum divergence of the stream-tube ahead of the measurement plane, as a result of the diffuser geometry, is <2.5° for the highest incidence considered. Similarly, the external fore-body geometry is based on a current intake design practice.

III. Reference flow-field

First, the reference flow-field, representative of an on-design take-off scenario, is assessed. Subsequently, the flow response to changes in both upper channel mass flow rate and angle of incidence is explored. All length-scales are non-dimensionalised using the maximum lip thickness at the throat t_m (see Figure 3).

A Schlieren photograph of the flow-field is shown in Figure 4a. Around the lip highlight, a very dark region is visible. This is likely to result from the optical distortion caused by very strong density gradients in this region. The bright area in Figure 4a is caused by the strong expansion in the supersonic domain. This is terminated downstream by a normal shock, which appears in the Schlieren photograph as a dark line approximately normal to the surface. Downstream of the shock, the boundary layer is clearly visible and can be seen to grow along the surface.

The RMS of light intensity fluctuations, obtained across a 1s sampling interval, is shown in Figure 4b. The region of high fluctuation intensity is strongly localised, implying minimal shock oscillation. From a qualitative point of view, the flow appears relatively benign and a λ-structure, typical of separated SBLI can not be observed from the Schlieren or fluctuation RMS image.

Figure 5 depicts centre-span LDV measurements taken to determine shock strength and position and to assess the boundary layer upstream of the shock. The stream-wise location of the shock in the inviscid core flow is taken as the point where M=1. From Figure 5b, this is found at $x_{shock} = 0.96t_m$, halfway between the highlight and the throat. The peak Mach number is measured to be $M_{max} = 1.5$. However, some degree of isentropic compression precedes the shock and the Mach number immediately upstream is found to be just over $M_{shock} = 1.4$. The wall normal measurement in Figure 5c was taken $0.09t_m$ upstream of the shock. Only two points could be obtained within the boundary layer and
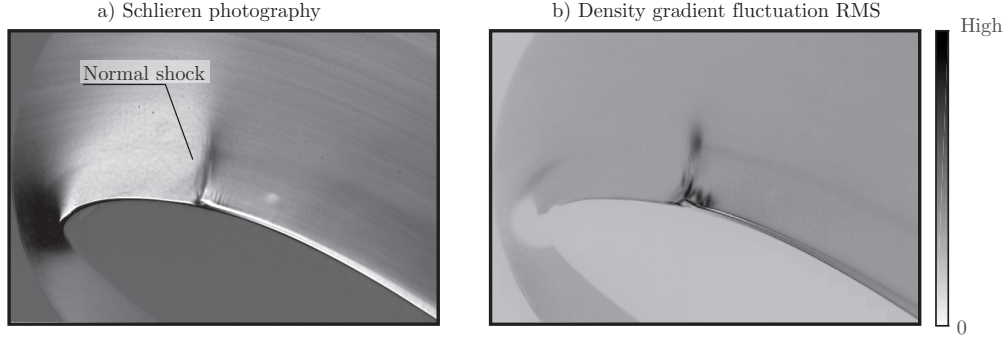
9

Fig. 4 a) Schlieren photograph of the flow-field at the reference conditions. Horizontal knife edge is used. b) RMS of light intensity from 4000 instantaneous Schlieren photographs captured over 1s. Scale applies solely to b).

therefore only an estimate of the boundary layer thickness could be obtained, suggesting that $\delta_1 \approx 0.024 t_m$.
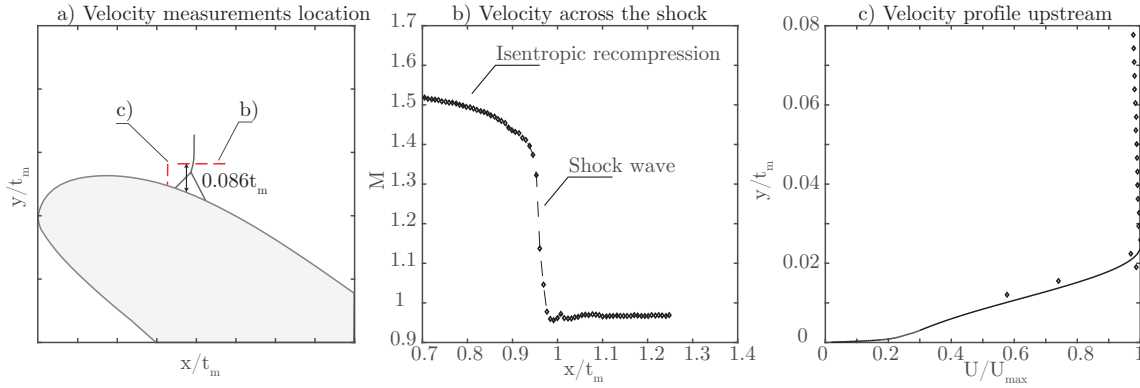

Fig. 5 a) Location of the LDV measurements in the tunnel centre span. b) Mach number variation in the core flow across the shock. c) Boundary layer measurement upstream of the shock.

A total of 11 wall normal velocity measurements have been performed using LDV around the shock wave in order to characterise the SBLI. The local Mach number contours are shown in Figure 6, along with the velocity fluctuations in the same region and a detail of the SBLI from the Schlieren image indicating the measurement location. The shock foot smearing onset coincides with a thickening of the boundary layer at approximately $3\delta_1$ upstream of the inviscid shock location (see annotation in Figure 6). This upstream influence is slightly greater than expected for an attached SBLI. Also, the shock Mach number is greater than the generally accepted separation boundary on flat plates (M=1.4) [23]. However, no distinct λ foot can be observed and negative velocities were not measured. It is noted, however, that LDV could not resolve the region $y \leq 0.2\delta_1$.

A surface oil flow visualisation image is presented in Figure 7. This suggests the presence of a small separation region underneath the shock foot. An accumulation of pigment, indicating a separation line, can be seen at s$\approx 0.9 t_m$ along the surface. A number of critical points, namely saddles and nodes, can be observed along the separation line.

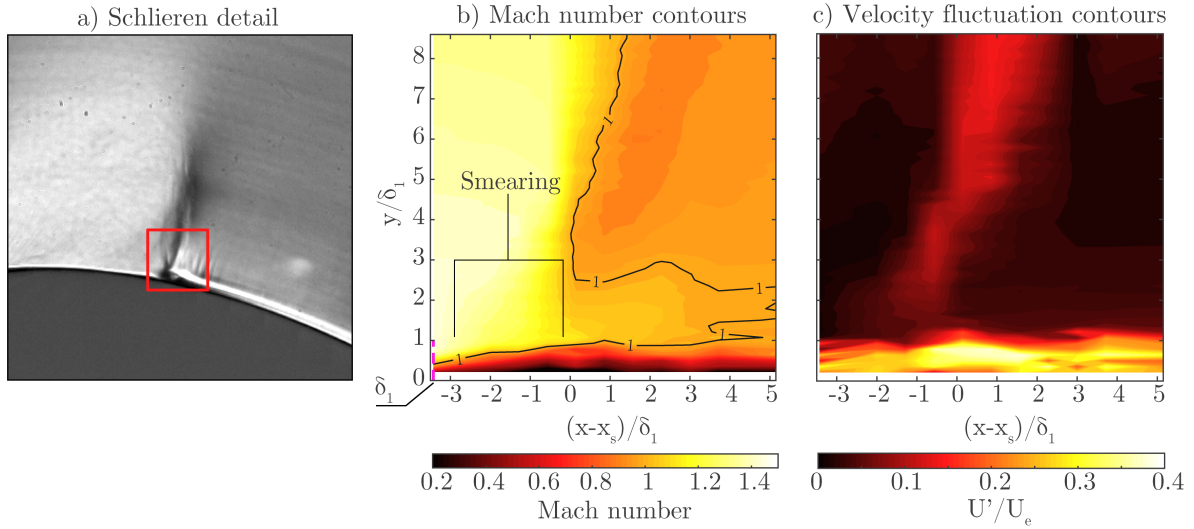a) Schlieren detail   b) Mach number contours   c) Velocity fluctuation contours

Fig. 6   a) Schlieren detail. b) Mach number contours from LDV. c) Contours of the velocity fluctuations.

Furthermore, two distinct *owl-face* [24] recirculating regions can be seen downstream. On both sides of these, separated regions can be faintly distinguished. Overall, the separation line shows a good degree of two-dimensionality. On the other hand, the reattachment is slightly three-dimensional and occurs at different stream-wise locations across the span.

The extent of separation ranges between $0.14t_m \leq L_{sep} \leq 0.17t_m$ across the central 80% of the span, which agrees well with the shock foot smearing observed in the velocity measurements and presented in Figure 6. The position of the stagnation point was also determined using oil flow and found at $s = -0.252t_m$ from the leading edge along the lower surface. Oil flow visualisation does not show any transition point or turbulent wedges and it is thus impossible to assert with certainty the *BL* nature. However, based on the shock Mach number M≥1.4 and the relatively benign interaction, the boundary layer is believed to be turbulent, thus capable of withstanding larger adverse pressure gradients without large scale separation.
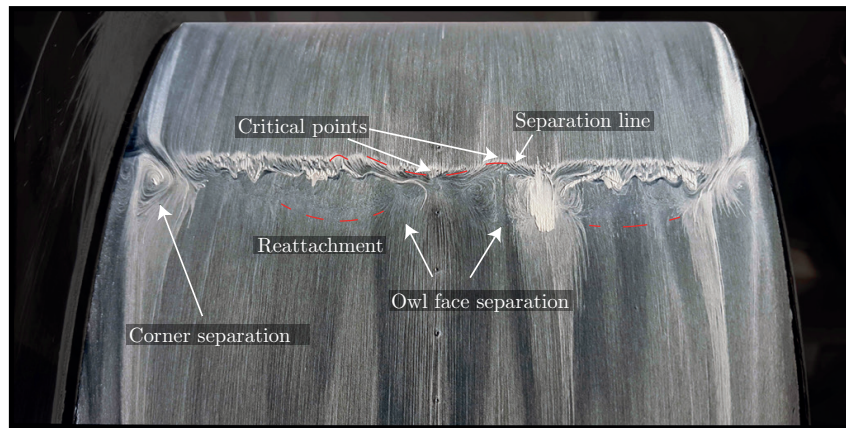

Fig. 7   Oil flow pattern for the on-design case.

11

Surface oil flow visualisation in Figure 7 also shows the extent of separation occurring near the junction between the model and the side-walls. On both extremes of the span, reversed flow can be observed from the streak-lines. Upon reaching the shock front, the boundary layer near the corner separates by similar mechanisms to those in the centre-span. The upstream influence is however greater and the separation line is swept back compared to the centre-span.

A primary concern with corner flow separations is their potential impact on centre-span separation development. Figure 8 is adapted from Bruce *et al.* [25] and shows how the separation boundary Mach number for a normal shock in rectangular channels increases with larger δ_1^*/w values, where w is the wind tunnel span (see Chapter 3). For a healthy boundary layer upstream of the shock, δ_1^* is not expected* to exceed $0.25\delta_1$, with $\delta_i^* \approx 0.15\delta_1$ being a reasonable estimate. This value for δ_1^*/w, included in Figure 8, suggests that a reasonably two dimensional flow can be expected with a fully developed turbulent separation for shock Mach numbers exceeding 1.3. Thus, the centre-span interaction is expected to be not significantly affected by corner effects, which is in agreement with the relatively 2D separation line seen in the surface oil visualisation. The presence of *owl-face* separations is more likely a result of secondary flow 'cells' developing inside the separated region.
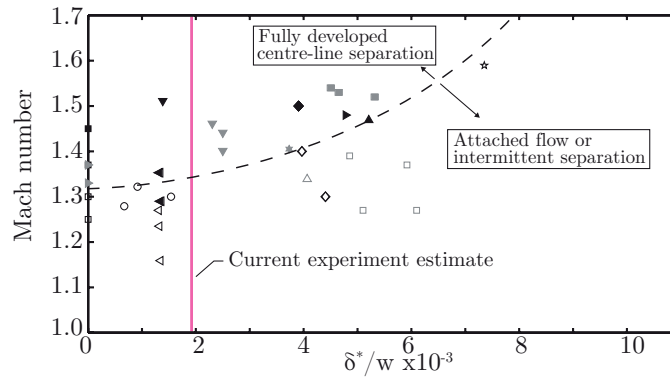

Fig. 8 Adapted from [25]. Experimental data for separated (filled symbols) and attached (open symbols) interactions: upstream Mach number vs δ^*/w.

Wall pressure measurements, obtained by a combination of pressure taps and PSP, are shown in Figure 9. Selected streamlines from the oil pattern in the separated region have been superimposed onto the pressure field to aid the interpretation. The pressure rise onset shows good agreement with the separation line and further confirms the two-dimensionality of the centre span flow. The black line in Figure 9b is the isentropic[†] sonic line, defined by a pressure ratio $P/P_0 = 0.528$. The relatively large distance between the pressure rise onset and the sonic line suggests that the shock-induced pressure rise is considerably smeared by the interaction. The extent of smearing is likely determined by the size of separation. The pressure gradient along the surface, extracted from the PSP, is plotted in Figure 9d. The stream-wise coordinate origin is taken at the inlet highlight. Following the initial expansion (dP/ds<0), upstream of

---

*for turbulent boundary layers and small dP/dx, $\theta \sim 0.1\delta$ [26, 27], for a healthy *BL*, $\delta^* \approx \theta$.

[†]assuming constant P_0 outside the boundary layer. As the shock near the BL edge is very weak [23], this assumption is deemed reasonable.

the shock (s≥ 0.5t_m) pressure gradients are seen to be adverse. This is consistent with the isentropic re-compression measured with LDV ahead of the shock wave (see Figure 5b). The peak isentropic surface Mach number is just below M=1.6, dropping just above M=1.4 immediately ahead of the shock. This is consistent with the velocity measurements in Figure 5. Downstream of the interaction, in the intake diffuser, as the flow is slowed down further before the nominal fan location, the pressure gradients are also measured to be adverse.
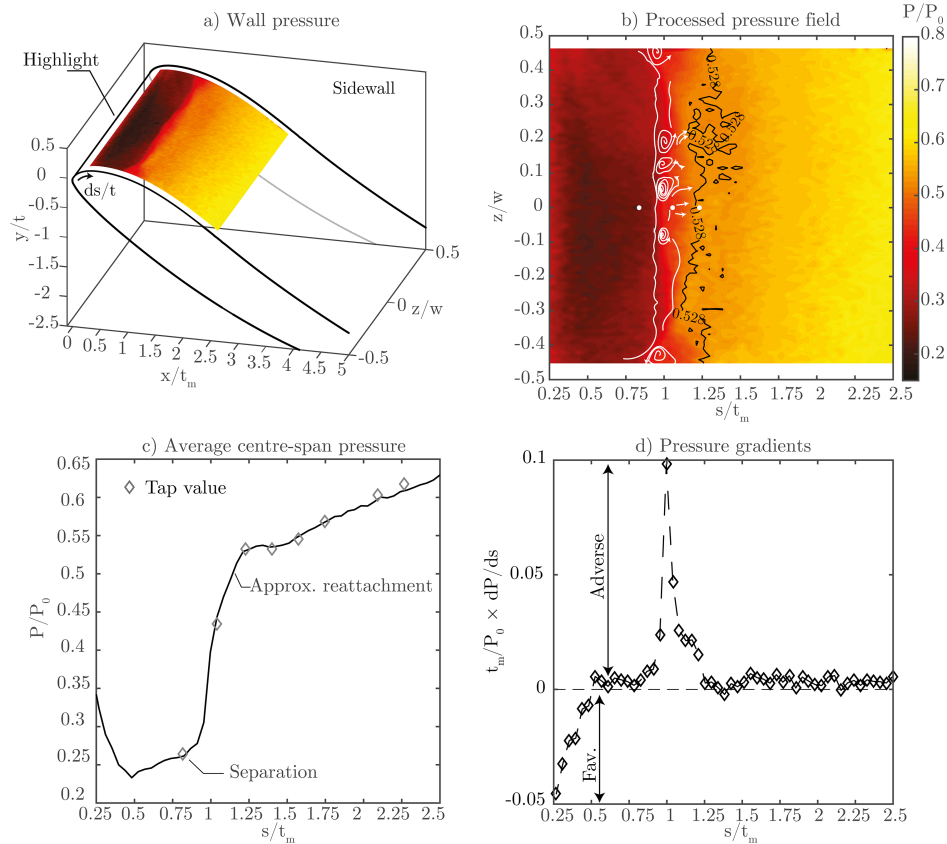

Fig. 9   a-b) Static wall pressure from PSP with streak-lines from oil flow superimposed. c) Pressure along the central span (average across 30% span), (◇) - tap values. d) Pressure gradients along centre-span.

Figure 10 shows three boundary layer velocity profiles, measured downstream of the interaction, in both physical parameters and also normalised by the local boundary layer thickness. The measurements were taken at a stream-wise distance from the highlight of x= 1.4t_m, 1.8t_m, 2.4t_m respectively, as indicated in Figure 10c. The furthest downstream location corresponds to the plane where an engine fan would sit.   This is slightly aft compared to the Aerodynamic Interface Plane, conventionally defined as slightly upstream of the fan plane. From now on, this location is referred to as the *Virtual Engine Plane (VEP)* and is used as a reference measurement plane for every flow condition tested. The boundary layer properties at the three stream-wise locations are summarised in Table 3.

At the first location, ∼ 20δ_1 downstream of the normal shock, the measured profile is typical for an equilibrium turbulent boundary layer with a shape factor of H_i = 1.277, suggesting a rapid recovery of the boundary layer after
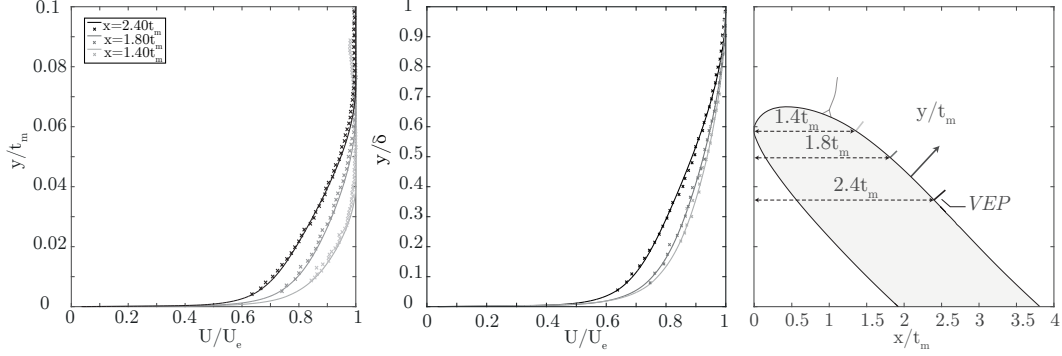
Fig. 10 a) **Wall normal velocity measurements. b) δ-normalised velocity profiles. c) Axial location of the wall normal measurement planes.**

Table 3   Boundary layer parameters at the three downstream locations.

Location (x)	δ/t_m	δ_i^*/t_m	θ_i/t_m	H_i
$1.40t_m$	0.041	0.004	0.003	1.277
$1.80t_m$	0.064	0.007	0.005	1.279
$2.40t_m$	0.074	0.010	0.0078	1.345

the separated SBLI. Progressing downstream, the velocity profile deteriorates and both displacement and momentum thicknesses increase. This is likely to be in response to the pressure rise in the diffuser. Nonetheless, at the *VEP*, $\sim 70\delta_1$ downstream of the normal shock, the shape factor $H_i = 1.345$ is still indicative of a healthy turbulent boundary layer.

IV. Increasing upper channel mass flow rate

In this section the effects of increasing the mass flow rate $\dot{m}_u$ in the wind tunnel upper channel (see Figure 11e for reference) at constant inflow Mach number and incidence are discussed. This is intended to replicate an increased demand by a turbofan engine.

Schlieren snapshots and fluctuation intensity RMS are shown in Figure 11a-d for all four upper channel mass flow rates considered (reference value, +4.9% $\dot{m}_u$, +9.8% $\dot{m}_u$, +14.7% $\dot{m}_u$). The baseline position of the shock wave is indicated by a dashed red line. At a glance, as the mass flow rate in the upper channel increases, the bright area outlining the supersonic region grows and the shock moves further downstream, closer to the intake throat. This is schematically portrayed in Figure 11e. Closer inspection of the Schlieren photographs in Figure 11 reveals a progressively more smeared shock foot as $\dot{m}_u$ increases. A distinct λ is not observed across the whole range. The density fluctuations, shown in the bottom row of Figure 11a-d, remain very localised for all mass flow ratios. This suggests the absence of significant large scale oscillations.

Schlieren and RMS in Figure 11 also show an oblique wave upstream of the normal shock for every $\dot{m}_u$ considered. This has been annotated in Figure 11d as it is most evident here. From Schlieren photographs, the straight line distance
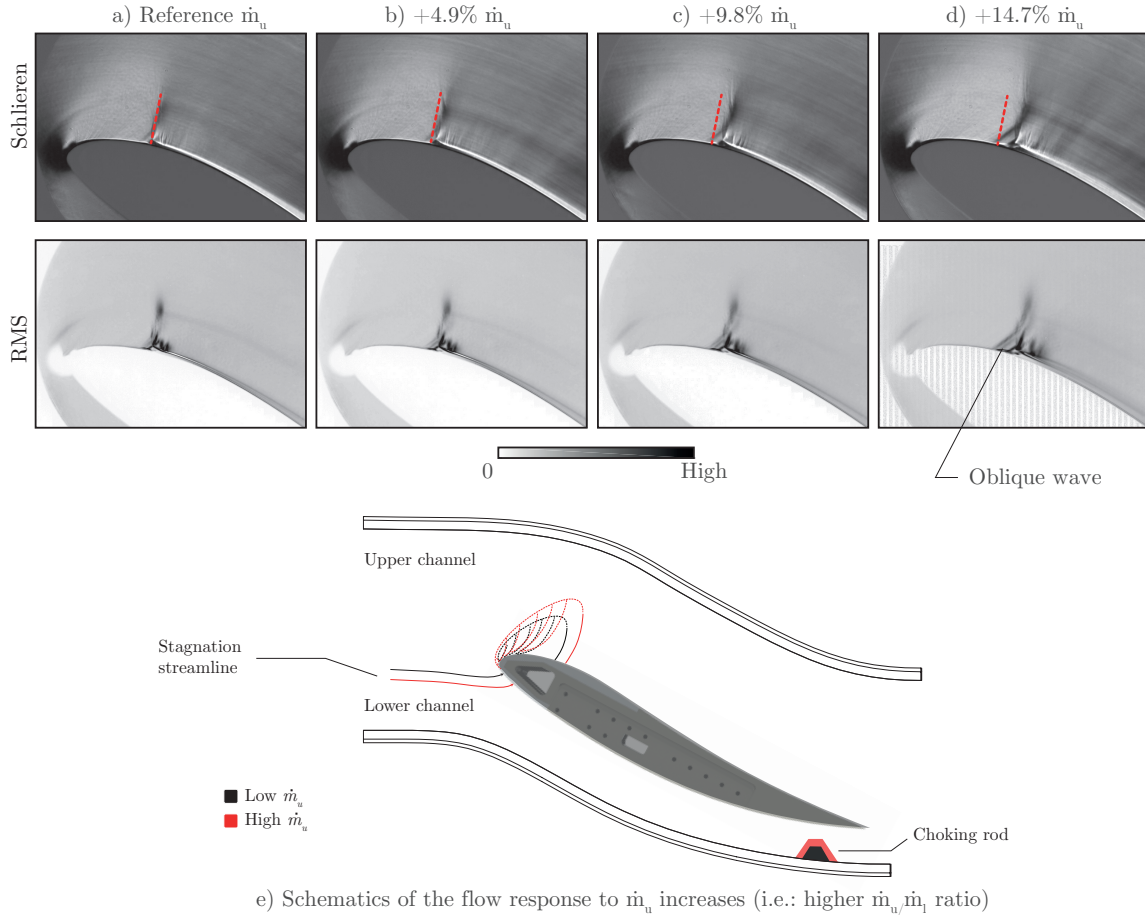
a) Reference $\dot{m}_u$ b) +4.9% $\dot{m}_u$ c) +9.8% $\dot{m}_u$ d) +14.7% $\dot{m}_u$

Schlieren

RMS

0   High

Oblique wave

Upper channel

Stagnation streamline

Lower channel

■ Low $\dot{m}_u$
■ High $\dot{m}_u$

Choking rod

e) Schematics of the flow response to $\dot{m}_u$ increases (i.e.: higher $\dot{m}_u/\dot{m}_l$ ratio)

Fig. 11   a-d) Schlieren snapshots (top) and density fluctuations (bottom) for the 4 increases in *engine* mass flow considered. e) Schematic depiction of the shock wave response to increases in $\dot{m}_u$.

(immediately above the wall) between the normal shock and this oblique wave is measured as $\sim 0.208t_m$ for the highest $\dot{m}_u$.

Pressure sensitive paint measurements are shown in Figure 12 for the reference mass flow rate and the largest increment. As $\dot{m}_u$ is increased by 14.7%, the centreline pressure jump moves $\Delta s \approx 0.2t_m$ further downstream compared to the baseline, consistent with the shock movement observed in the Schlieren images. Near the corners, a greater sweep of the pressure jump line is observed at this higher mass flow rate. Here, the stream-wise distance between the onset of pressure jump in the corner and in the centre-span is $\sim 0.217t_m$ for the highest $\dot{m}_u$. This distance is consistent with that measured between the normal shock and the oblique wave in the Schlieren photograph (Figure 11e). Based on this evidence, it seems likely that the oblique wave is the front leg of the corner SBLI [28].

Figure 12 includes streamlines from oil flow visualisation[‡] for both $\dot{m}_u$ values. It can be seen that the separated region increases with $\dot{m}_u$, reaching ~twice the size of the baseline separation for the largest $\dot{m}_u$. Interestingly, there is a good correlation (around the central region) between the reattachment line observed from oil flow visualisation and the

---

[‡]For the baseline oil pattern see Figure 7, for the high $\dot{m}_u$ one see Appendix.

isentropic sonic line determined from PSP. This could be explained by a secondary supersonic pocket forming over the separation bubble downstream of the shock; as the flow reattaches, the boundary layer edge velocity sharply drops below M=1. Thus, the isentropic sonic line can be used together with the pressure rise onset to obtain a reasonable (upper) estimate of the separation extent.
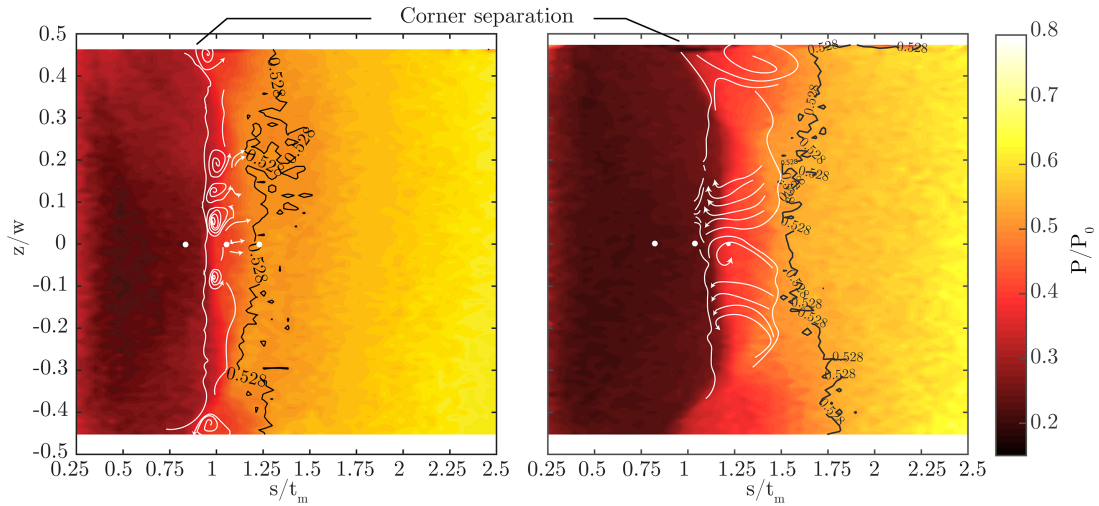

Fig. 12   Wall pressure from PSP with superimposed streak-lines for reference $\dot{m}_u$ (left) and highest increment (15% - right).

Figure 13 shows velocity measurements taken across the inviscid core flow above the interaction. As $\dot{m}_u$ is increased, the downstream motion of the shock is accompanied by a progressively higher peak Mach number, which exceeds M= 1.6 for the largest $\dot{m}_u$. Some degree of isentropic re-compression is observed in every case. As a result, the Mach numbers immediately upstream of the shocks are lower than the maximum measured values. From Figure 13, the shock Mach number is seen to be around M ~ 1.5 for the largest mass flow rate considered.
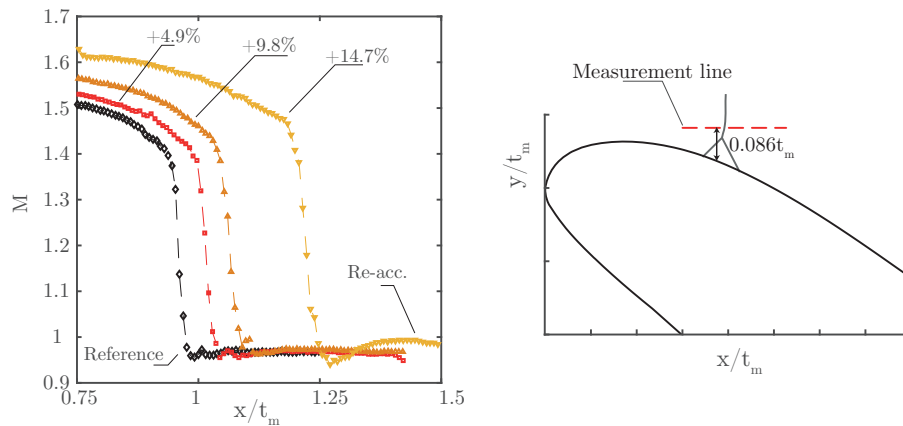

Fig. 13   Velocity measurements across the inviscid shock for increasing $\dot{m}_u$.

The boundary layer profiles at three locations are shown in Figure 14 and the corresponding integral properties are summarised in Table 4. To aid clarity, the raw data is only included for the baseline as this is representative of the agreement with the analytical model; for all other profiles only the analytical fit is given[§]. As an exception, the velocity measurements taken at the most upstream plane (x= $1.40t_m$) for the highest $\dot{m}_u$ are included as well. In this particular case the boundary layer appears distorted and measurements show considerable divergence from the fitted model. This is likely a consequence of the proximity to the reattachment point, where the theoretical profile is unlikely to fit well. Furthermore, a greater scatter is seen as the reattachment is likely to be more unsteady. As a result, the integral parameter estimates for this case should be treated with caution. Nonetheless, despite the considerable distortion of the boundary layer so close to the SBLI, the boundary layer for the highest $\dot{m}_u$ is seen to recover quickly. In particular, at $x/t_m = 1.80$ the measured shape factor is $H_i = 1.264$, indicative of a very healthy boundary layer. Further downstream, at the *VEP* a trend of decreasing shape factor with increasing mass flow rate is seen (Table 4). Although the differences are small and could be deemed within experimental error, the trend is consistent and, while counter-intuitive at first, this behaviour can potentially be explained from the stream-wise development of shape factor as shown in Figure 15b. At separation, shape factor increases rapidly to very high values as the velocity profile distorts. Upon reattachment, the boundary layer experiences a strong rehabilitation phase during which H_i drops sharply towards pre-shock values. Such behaviour is typical for transonic SBLIs [23]. However, as shown in Figure 15a, there is a considerable pressure rise in the following diffuser section. Consequently, at some distance downstream of reattachment, the boundary layer integral parameters increase again in response to the adverse pressure gradients, following the curves shown in Figure 15b. When the shock moves downstream with higher $\dot{m}_u$, the local minimum shifts closer to the *VEP* and the boundary layer experiences a shorter distance of adverse pressure gradients. This provides an explanation for the measured shape factor decreasing with increasing mass flow. Overall, at the *VEP*, every velocity profile measured is representative of a healthy turbulent boundary layer.

Table 4   Boundary layer parameters at the three downstream locations.

(a) Reference $\dot{m}_u$

Loc.	δ/t_m	δ_i^*/t_m	θ_i/t_m	H_i
$1.40t_m$	0.041	0.004	0.003	1.277
$1.80t_m$	0.064	0.007	0.005	1.279
$2.40t_m$	0.074	0.010	0.0078	1.345

(b) +4.9% $\dot{m}_u$

Loc.	δ/t_m	δ_i^*/t_m	θ_i/t_m	H_i
$1.40t_m$	0.041	0.0044	0.0034	1.297
$1.80t_m$	0.062	0.0073	0.0056	1.299
$2.40t_m$	0.075	0.010	0.0077	1.333

(c) +9.8% $\dot{m}_u$

Loc.	δ/t_m	δ_i^*/t_m	θ_i/t_m	H_i
$1.40t_m$	0.039	0.0045	0.0034	1.308
$1.80t_m$	0.061	0.0065	0.0051	1.282
$2.40t_m$	0.078	0.010	0.0076	1.317

(d) +14.7% $\dot{m}_u$

Loc.	δ/t_m	δ_i^*/t_m	θ_i/t_m	H_i
$1.40t_m$	0.034	0.0075	0.0048	1.575
$1.80t_m$	0.064	0.0073	0.0058	1.264
$2.40t_m$	0.087	0.010	0.008	1.297

[§]the raw data for every wall normal measurement are available in Appendix A.
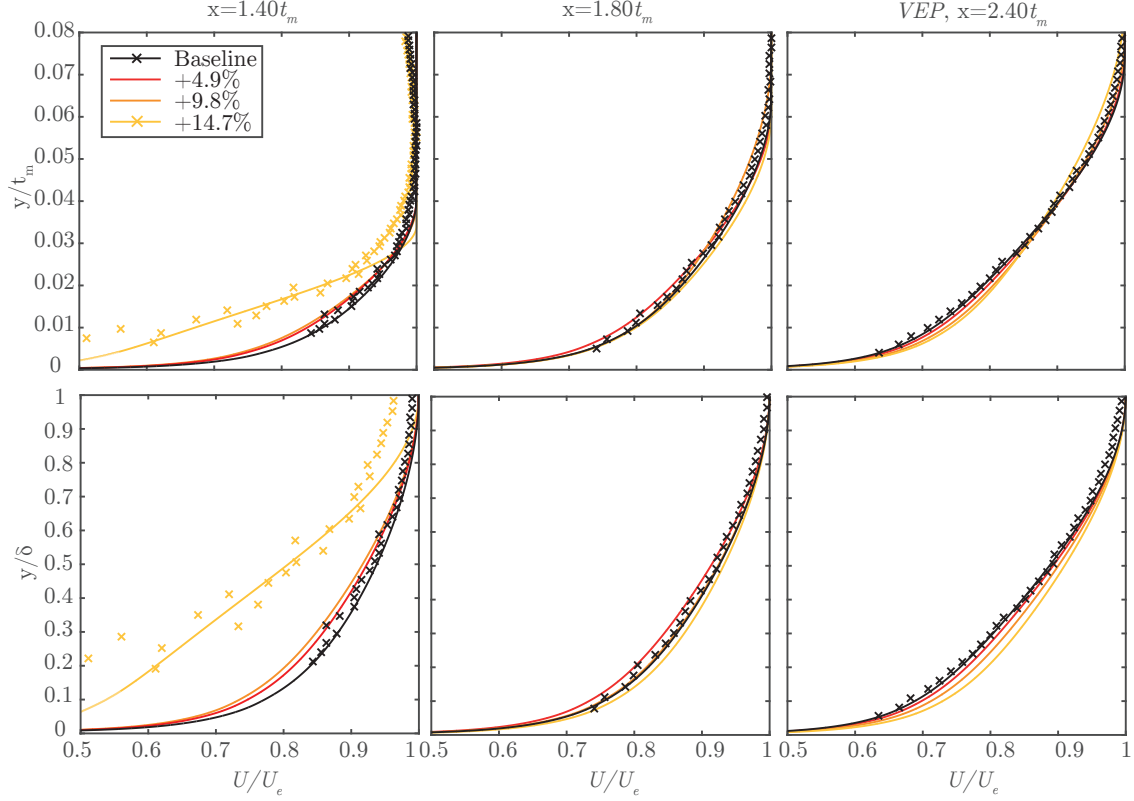
Fig. 14   Boundary layer development for the upper channel mass flow range considered.

V. Increasing incidence

Beyond the reference angle of 23°, two more incidence levels have been considered, namely 25° and 26°. Initially, the ratio $\dot{m}_u/\dot{m}_l$ is set to the same level as the baseline (within 4%). Then, the consequences of a greater upper channel mass flow rate at higher incidence are also investigated.

A number of Schlieren snapshots for the reference mass flow rate are shown in Figure 16, along with the corresponding time averaged images (1s, 4000 frames).

As the incidence is increased, the flow becomes unsteady and significant stream-wise shock motions are observed at 25° and 26°. From the instantaneous Schlieren images on the left of Figure 16, at higher incidence, a λ foot, suggesting shock-induced separation, can be observed across the whole range of shock motion. The size of the λ foot is most prominent for the highest incidence of 26° and it is seen to vary as the shock oscillates along the surface. Observing the time averaged images, a greater smearing of the interaction is seen at 26° compared to 25°, suggesting a more pronounced shock motion. The spatial extent of shock oscillation can be more easily inferred from the fluctuation RMS, shown with time averaged Schlieren images in Figure 17 for both the reference and highest $\dot{m}_u$. A progressively greater degree of stream-wise smearing can be observed with increasing incidence. In contrast, the extent of shock oscillations appears to increase only slightly with $\dot{m}_u$.
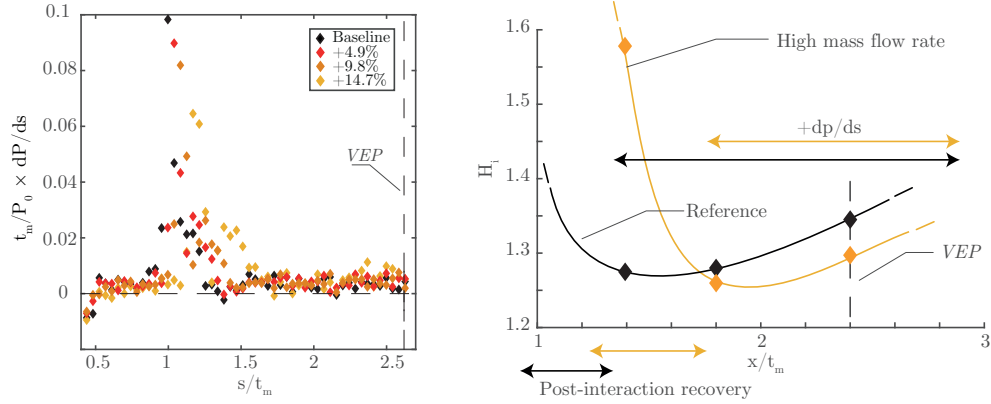
Fig. 15 Suggested mechanism by which a lower shape factor is measured at the *VEP* despite a closer and more severe interaction.
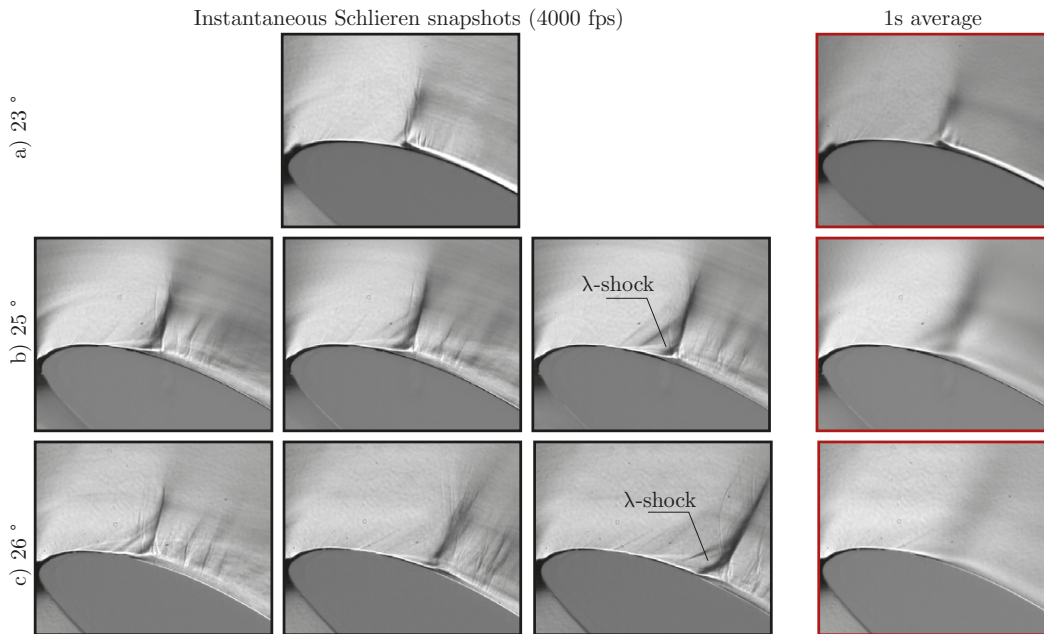

Fig. 16 Selected Schlieren snapshots (1/4000s exposure) and 1s-time average at three incidence levels for reference upper channel mass flow.

Time-averaged wall static pressure, captured using PSP[¶], is shown in Figure 18. At 25° and 26° the onset of pressure rise in the centre-span is found at a stream-wise position along the surface $s_s \approx 0.9t_m$. This is similar to the baseline incidence. The estimated mean separation size, as indicated by the distance between the shock and the isentropic sonic line, grows progressively in size with incidence. Furthermore, a progressively more extensive region of smeared pressure near the corners is observed at higher angle of attack.

In contrast to the observations at the baseline incidence of 23°, mean wall pressure does not show significant response to $\dot{m}_u$ increases at both increased angles of attack.

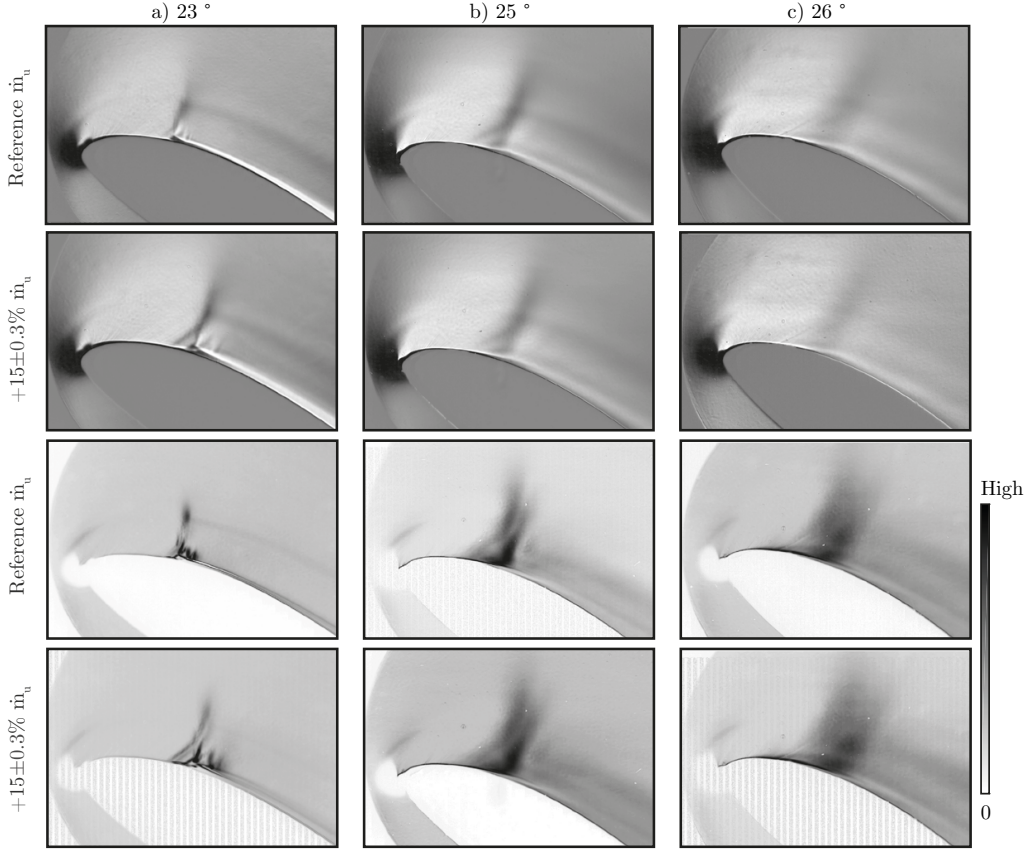[¶]exposure time ~50 times the dominant oscillation period.

Fig. 17   1 second average of 4000 Schlieren snapshots and light intensity RMS for increasing incidence and $\dot{m}_u$.

Stream-wise velocity measurements across the shock are shown in Figure 19. These were taken above the bifurcated part of the λ shock observed in the Schlieren photographs in Figure 16. The shock Mach number is approximately M $\approx$ 1.6 for both higher incidence levels. A greater degree of unsteadiness at 26° is reflected by a greater smearing of the velocity measurements across the shock[||]. For both high incidence scenarios the velocity data show a modest re-acceleration of the flow downstream of the shock-wave, likely occurring over the convex, separated, boundary layer. Furthermore, consistent with flow visualisation and pressure measurements, there is little variation in the shock position with increasing $\dot{m}_u$, especially when compared to the behaviour at 23°. Similarly, increases in Mach number with $\dot{m}_u$ are considerably less prominent than at the reference incidence.

Velocity profiles at the *VEP* are shown in Figure 20. The integral parameters for all incidences and mass flow rates are summarised in Figure 21 and Table 5. A considerable effect of angle of incidence is observed. In particular, the boundary layer thickness is seen to increase noticeably compared to the reference case, by ~130% at 25° and more than 190% at 26°.

Measurements normalised by outer units, given in Figure 20b, show a progressive deterioration of the velocity

---

[||]Each point was averaged across 0.2s, corresponding to approximately 20 cycles of the main oscillation period
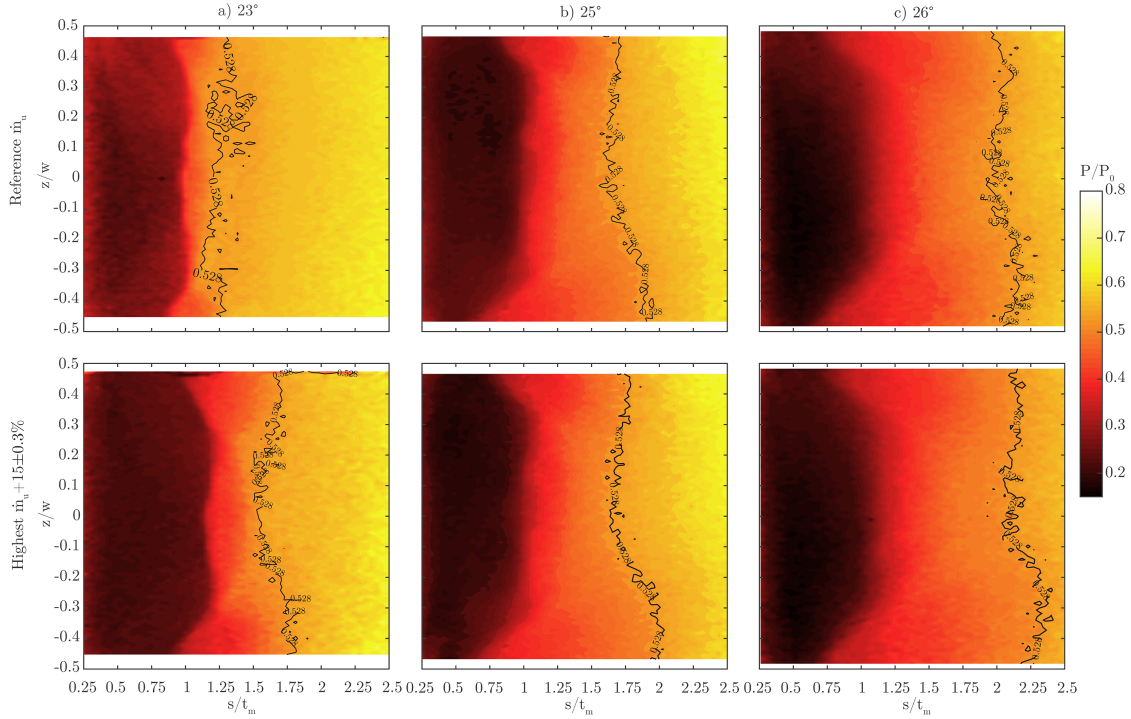
Fig. 18   Wall pressure along model surface for increasing incidence and $\dot{m}_u$.

profile as incidence is increased. The shape factor rises from the reference value of $H_i = 1.345$ to a maximum value of $H_i = 1.930$ for the highest incidence of $26°$, which is indicative of a very unhealthy boundary layer. This might be caused by a combination of the greater separation size and the reattachment having occurred only a short distance upstream of the *VEP*. The profiles normalised in wall units are shown in Figure 20c. For $23°$ and $25°$, measured velocities show a reasonable collapse in the logarithmic region. Above $y^+ \geq 1000$, the velocity profiles reflect the larger pressure gradients with a more pronounced wake region.

As shown in Figure 21, for all incidence levels, there is little change in boundary layer parameters with upper channel mass flow rate $\dot{m}_u$. Due to the less robust fit of the analytical model, these variations are deemed within experimental error.

Overall, although both increases in incidence and in 'engine' mass flow rate have as a consequence an outward movement (along the external fore-body) of the stagnation point, from the findings reported in §IV and V, there appears to be a noticeably more severe flow response to incidence. In particular, higher incidence results in severe distortion of the velocity profile at the nominal fan location. This is likely a consequence of the more extensive separation reported at $25°$ and $26°$, potentially resulting from a more aggressive post-shock diffusion downstream inhibiting the reattachment process. Furthermore, at higher incidence levels, the flow sensitivity to changes in $\dot{m}_u$ is reduced further. This is currently attributed to the de-cambering effect by the largely separated boundary layer downstream of the shock preventing any forward movement of the shock, which is observed at lower incidence.
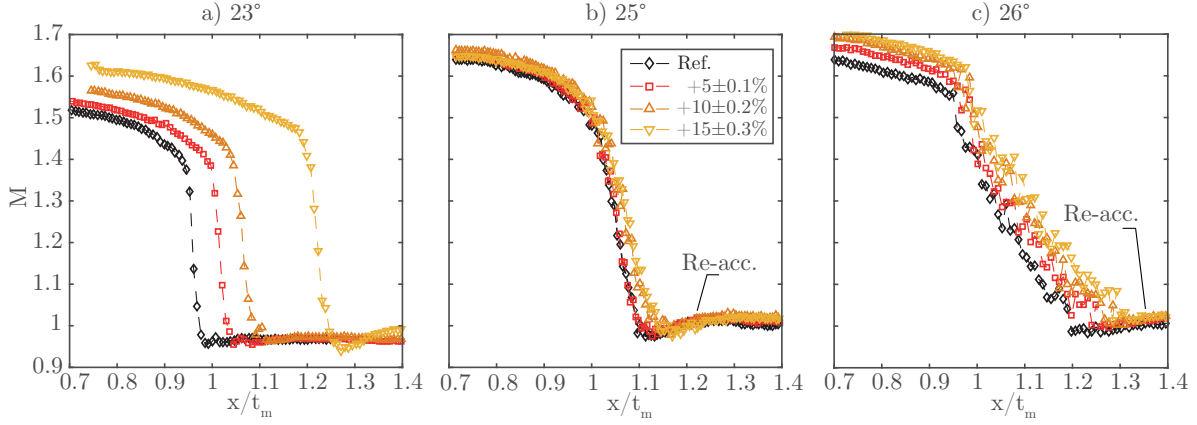
21

Fig. 19 Stream-wise velocity measurements in the core flow for the range of incidences and upper channel mass flow rates. The measurement was taken immediately above the interaction.
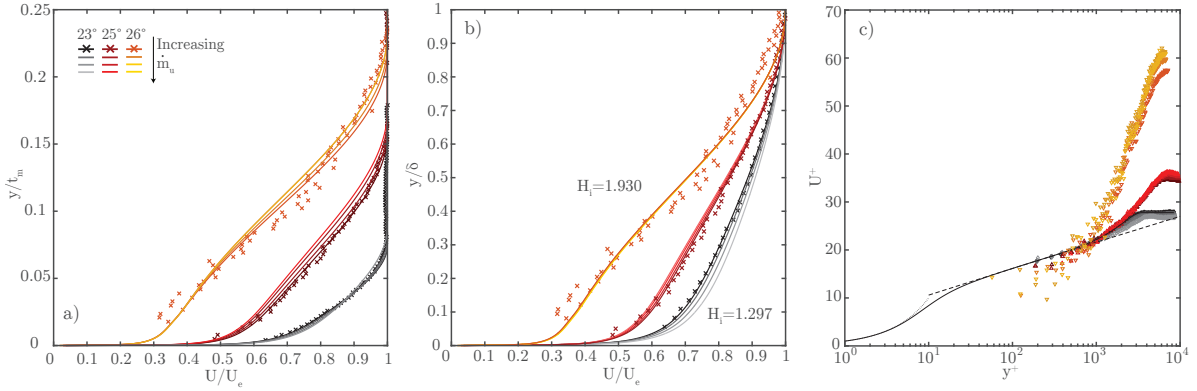

Fig. 20 a) Wall normal velocity measurements at the *VEP*. b) δ-normalised boundary layer velocity profiles for the range of incidences and $\dot{m}_u$ considered. c) Law of the wall for the range of incidences and $\dot{m}_u$ considered.
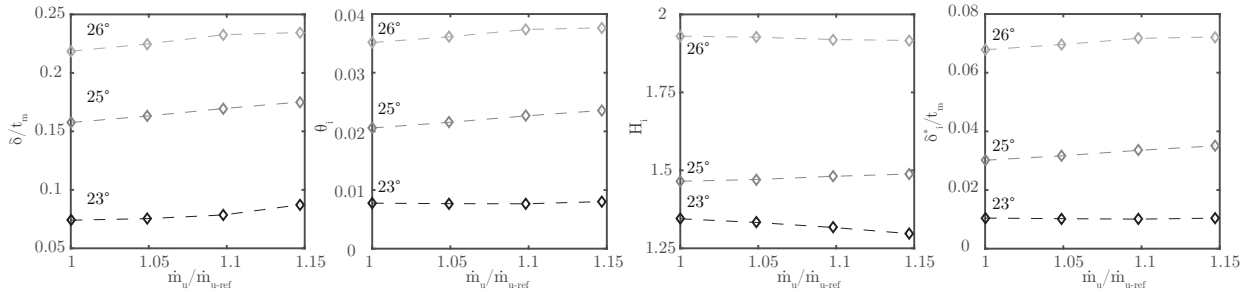

Fig. 21 Variation in boundary layer integral properties with incidence and upper channel mass flow rate.

VI. Conclusion

Using a novel experimental rig, the shock-wave boundary layer interaction over the lower lip of a transonic inlet was studied in detail for a range of inflow conditions representative of high-incidence manoeuvres.

The wind-tunnel entry Mach number is set at M=0.435. As for transonic aerofoils, a strong effect of free-stream Mach number on the strength and location of the shock is expected. The Mach number used herein is indicative of edge

Table 5 Incompressible boundary layer parameters for all α and $\dot{m}_u$ at the *VEP*.

(a) Reference $\dot{m}_u$

$\alpha(°)$	δ/t	δ_i^*/t	θ_i/t	H_i
23	0.074	0.010	0.0078	1.345
25	0.158	0.030	0.0210	1.465
26	0.219	0.068	0.0351	1.930

(b) +4.9% $\dot{m}_u$

$\alpha(°)$	δ/t	δ_i^*/t	θ_i/t	H_i
23	0.075	0.010	0.0077	1.333
25	0.163	0.032	0.0215	1.471
26	0.225	0.070	0.0361	1.927

(c) +9.8% $\dot{m}_u$

$\alpha(°)$	δ/t	δ_i^*/t	θ_i/t	H_i
23	0.078	0.010	0.0076	1.317
25	0.169	0.033	0.0226	1.481
26	0.233	0.072	0.0374	1.921

(d) +14.7% $\dot{m}_u$

$\alpha(°)$	δ/t	δ_i^*/t	θ_i/t	H_i
23	0.087	0.010	0.008	1.297
25	0.175	0.035	0.0236	1.488
26	0.235	0.072	0.0377	1.918

of the envelope operations; exploring a wider range of Mach numbers was beyond the scope of the current investigation. Three incidence levels were considered, namely the reference case of 23°, and two 'off-design' conditions at 25° and 26° respectively. Furthermore, increases mass flow rate over the lip up to 15% of the initial value have also been considered.

For the reference case, a M~1.4 shock-wave is present. Despite the relatively high Mach number, the interaction is found to be benign in nature with only minor shock-induced separation observed. Downstream of the reattachment point, velocity measurements show that, despite the adverse pressure gradients defining the inlet diffuser, the boundary layer recovers quickly and at the nominal fan location the velocity profile is that of an equilibrium turbulent boundary layer. Increases in mass flow rates did not hinder the subsequent recovery of the boundary layer. In particular, although the shock gets stronger, this moves closer to the nominal engine face, resulting in the adverse pressure gradient in the diffuser being 'felt' over a shorter distance after reattachment.

Changes in the angle of incidence have a far greater impact on the intake performance. Increasing the incidence to 25° results in a stronger shock-wave and in the onset of large scale shock oscillation. This is exacerbated at the highest incidence considered (26°). Furthermore, the size of shock induced separation appears progressively larger. This could be attributed to a more aggressive post-shock diffusion downstream of the shock resulting from the higher incidence which inhibits flow reattachment. This is ultimately reflected in a severe deterioration of the boundary layer, with a momentum thickness growing up to 350% compared to the reference case.

Appendix

A. Wall normal velocity measurements

For the vast majority of velocity measurements, only the fitted models were presented in the main body to avoid cluttering in the plots. The raw data was included for selected cases, representative of the agreement between measurements and fitted models.

Every wall normal velocity measurement is presented here. No scaling has been applied and raw data is shown for

each case. The fitted model is also included.

Figure 22 shows wall normal velocity measurements at three locations for the baseline case at $23°$ and at the *VEP* for the two higher incidence cases. Four upper channel mass flow rates are included.
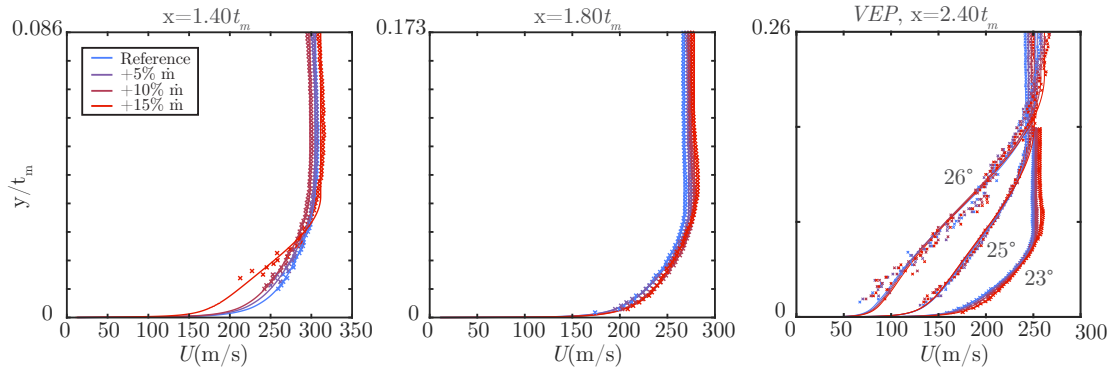

Fig. 22   Wall normal velocity measurements used in the main text. Four values of $\dot{m}_u$ included.

B. Baseline lip-high $\dot{m}_u$ oil flow vis.

Streamline from oil flow visualisation are depicted in Figure 12 superimposed onto the pressure field. The pattern from which those were extracted is shown in Figure 23.

Fig. 23   Oil flow visualisation at $23°$ for the highest $\dot{m}_u$ considered, +15% over the reference value.

Acknowledgements

References

[1] EUROPEAN-COMMISSION, *Flightpath 2050 - Europe's Vision for Aviation*, Publishing Office of the European Union, Luxembourg, 2011. doi:10.2777/50266.

[2] VIALL, W. S., "The Engine Inlet on the 747," *ASME 1969 Gas Turbine Conference and Products Show*, 1969. doi: 10.1115/69-GT-41.

[3] MILLER, B. A., and DASTOLI, B. J., "Effect of entry lip design on aerodynamics and acoustics of high-throat- Mach-number inlets for the quiet, clean, short-haul experimental engine." *NASA Technical Paper 3222*, 1975.

[4] JAKUBOWSKI, A. K., and LUIDENS, R., "Internal cowl-separation at high incidence angles," *13th Aerospace Sciences Meeting. Pasadena,CA,USA.*, 1975. doi:10.2514/6.1975-64.

[5] ALBERS, J. A., and MILLER, B. A., "Effect of Subsonic Inlet Lip Geometry On Predicted Surface and Flow Mach Number Distributions," *NASA Technical Note 7446*, 1973.

[6] CHOU, D. C., LUIDENS, R. W., and STOCKMAN, N. O., "Prediction of Boundary-Layer Flow Separation in V/STOL Engine Inlets," *Journal of Aircraft*, Vol. 15, No. 8, 1978, pp. 474–481. doi:10.2514/3.58393.

[7] KENNEDY, S., ROBINSON, T., SPENCE, S., and RICHARDSON, J., "Computational Investigation of Inlet Distortion at High Angles of Attack," *Journal of Aircraft 2014 51:2, 361-376*, 2014. doi:10.2514/1.C031789.

[8] CAO, T., NAGABHUSHANA, R. V., TUCKER, P. G., ANGUS, R., SLABY, M., and SHEAF, C. T. J., "Fan–Intake Interaction Under High Incidence," *J. Eng. Gas Turbines Power 139(4), 041204*, 2016. doi:10.1115/1.4034701.

[9] MAKUNI, T. E., BABINSKY, H., SLABY, M., and SHEAF, C. T., "Shock Wave-Boundary-Layer Interactions in Subsonic Intakes at High Incidence," *53rd AIAA Aerospace Sciences Meeting. January*, 2015. doi:10.2514/6.2015-0067.

[10] DAGGET, D. L., BROWN, S. T., and KAWAI, R. T., "Ultra-Efficient Engine Dimaeter Study," *NASA Technical Report No. 212309*, 2003.

[11] RAYLE, R., "An investigation of the influence of orifice geometry on static pressure measurements," Master's thesis, Massachusetts Institute of Technology, 1949.

[12] GREGORY, J. W., ASAI, K., KAMEDA, M., LIU, T., and SULLIVAN, J. P., "A review of pressure-sensitive paint for high-speed and unsteady aerodynamics," *Proc. IMechE Vol. 222 Part G: J. Aerospace Engineering*, 2007. doi:10.1243/09544100JAERO243.

[13] COLLISS, S. P., *Vortical structures on three-dimensional shock control bumps*, PhD Thesis, University of Cambridge, 2014.

[14] SHAKAL, J., and TROOLIN, D., "Accuracy, Resolution, and Repeatability of Powersight PDPA and LDV Systems," *TSI Technical Note P/N 5001519*, 2013.

[15] MCLAUGHLIN, D. K., and TIEDERMAN, W. G., "Biasing correction for individual realization of laser anemometer measurements in turbulent flows," *Physics of Fluids*, Vol. 16, No. 1973, 1973, pp. 2082–2088. doi:10.1063/1.1694269.

[16] BUCHHAVE, P., and GEORGE, W. J., "Bias corrections in turbulence measurements by the laser Doppler anemometer," Tech. rep., Turbulence Research Laboratory, State University of New York at Buffalo, 1978.

[17] SUN, C., and CHILDS, M. E., "A modified wall wake velocity profile for turbulent compressible boundary layers." *Journal of Aircraft*, Vol. 10, No. 6, 1973, pp. 381–383. doi:10.2514/3.44376.

[18] COLES, D., "The law of the wake in the turbulent boundary layer," *Journal of Fluid Mechanics*, Vol. 1, No. 02, 1956, p. 191. doi:10.1017/S0022112056000135.

[19] MUSKER, A. J., "Explicit Expression for the Smooth Wall Velocity Distribution in a Turbulent Boundary Layer," *AIAA Journal*, Vol. 17, No. 6, 1979, pp. 655–657. doi:10.2514/3.61193.

[20] TITCHENER, N., COLLISS, S., and BABINSKY, H., "On the calculation of boundary-layer parameters from discrete data," *Experiments in Fluids*, Vol. 56, No. 8, 2015, pp. 1–18. doi:10.1007/s00348-015-2024-5.

[21] LIN, N., REED, H. L., and SARIC, W. S., "Effect of leading-edge geometry on boundary-layer receptivity to freestream sound," *Instability, Transition, and Turbulence*, 1992, pp. 421–440. doi:10.1007/978-1-4612-2956-8_42.

[22] SCHRADER, L.-U., BRANDT, L., MAVRIPIIS, C., and HENNINGSON, D. S., "Receptivity to free-stream vorticity of flow past a flat plate with elliptic leading edge," *Journal of Fluid Mechanics*, Vol. 653, 2010, pp. 245–271. doi: 10.1017/S0022112010000376.

[23] BABINSKY, H., and HARVEY, J. K., *Shock-wave-Boundary layer Interactions*, Cambridge University Press, 2011. doi: 10.1017/CBO9780511842757.

[24] PERRY, A., and HORNUNG, H., "Some aspects of three-dimensional separation. II - Vortex skeletons," *Zeitschrift fur Flugwissenschaften und Weltraumforschung*, Vol. 8, 1984, pp. 155–160.

[25] BRUCE, P. J. K., BURTON, D. M. F., TITCHENER, N., and BABINSKY, H., "Corner effect and separation in transonic channel flows," *Journal of Fluid Mechanics*, Vol. 679, 2011, pp. 247–262. doi:10.1017/jfm.2011.135.

[26] WHITE, F. M., *Viscous Fluid Flow, Third Edition*, McGraw Hill, 2006.

[27] YOUNG, A., *Boundary layers*, AIAA Education Series, 1989.

[28] BURTON, D. M. F., and BABISNKY, H., "Corner separation effects for normal shock wave/turbulent boundary layer interactions in rectangular channels," *Journal of Fluid Mechanics*, Vol. 707, 2012, pp. 287–306. doi:10.1017/jfm.2012.279.